Journal of Materials Chemistry C

ROYAL SOCIETY OF CHEMISTRY

PAPER

View Article Online
View Journal | View Issue

Cite this: J. Mater. Chem. C, 2025, 13, 10780

A simple medium-bandgap quinoidal A–D–A non-fullerene acceptor for ternary organic solar cells†

Shyam Shankar S.,[a] María Privado,[b] Pilar de la Cruz, *[b] Fernando Langa *[b] and Ganesh D. Sharma *[a]

Received 19th February 2025,
Accepted 21st April 2025

DOI: 10.1039/d5tc00724k

rsc.li/materials-c

The composition of the bulk heterojunction active layers in organic solar cells is crucial to their photovoltaic performance. Highly efficient organic solar cells have been constructed by the so-called ternary approach due to its process simplicity and diverse donor and acceptor materials. In the study described here, the simple medium-bandgap closed-shell quinoidal A–D–A non-fullerene small molecule acceptor **QDT1**, *i.e.*, 4,4-dihexyl-4*H*-cyclopenta[2,1-*b*:3,4-*b*′]dithiophene (CPDT), was used as a guest acceptor in the PBDB-T:Y6 host binary active layer to fabricate ternary organic solar cells. **QDT1** has an absorption profile that is complementary to those of the host active materials (PBDB-T and Y6). This matching of profiles is beneficial for light-harvesting and ultimately enhances the photocurrent in the OSC devices. Ternary organic solar cells fabricated in ambient conditions with the optimized PBDB-T : **QDT1** : Y6 (1.0 : 0.2 : 1.0) active layer gave an overall power conversion efficiency of 13.31%, which is better than that of the PBDB-T:Y6 counterpart (11.17%). The higher PCE in the ternary system is mainly attributed to the higher short circuit photocurrent and fill factor along with a decreased energy loss. The increases in photocurrent and fill factor can both be attributed to faster exciton dissociation, energy transfer from **QDT1** to Y6, more rapid charge extraction, extended charge carrier lifetime and lower charge recombination. The organic solar cells based on a PBDB-T:**QDT1** active layer provided a PCE greater than 23% under indoor illumination (white LED).

Introduction

Organic solar cells (OSCs) have several advantages over silicon-based solar cells and these include flexibility, a lightweight structure, and the possibility of cost-effective applications in wearable electronic devices, indoor internet of things and building integrated photovoltaics.[1–6] In recent years the emergence of non-fullerene acceptors (NFAs)[7–11] has led to significant advances in OSCs and the power conversion efficiency (PCE) has reached 20%.[12–17] The most effective OSCs generally consist of bulk heterojunction (BHJ) blend layers that consist of electron donors (D) and acceptors (A). In these layers the hierarchical blend structures tend to incorporate interpenetrated D/A nanoscale networks to enhance the exciton dissociation into free charge carriers and their subsequent transport towards electrodes.[18,19] The majority of OSCs are based on NFAs but the synthesis of these materials involves complex and lengthy procedures, which result in substantial expenses that create major obstacles for industrialization of OSCs.

In recent years non-fused-ring NFAs have emerged as competitive low-cost materials for OSCs due to their simple synthesis routes.[20–23] OSCs based on non-fused NFAs have given a PCE value of 17% for a binary BHJ active layer[24–26] and 18% for a ternary active layer,[27] which is very close to the values obtained for fused-ring NFAs.

Despite the remarkable properties of quinoidal semiconductors and the fact that they are already used in organic transistors,[28,29] their application as electron acceptors in organic solar cells (OSCs) remains limited.[30,31] The incorporation of quinoidal structures, however, provides an alternative approach to developing high-performance electron acceptors owing to several exclusive advantages: (i) the rigid and flat configuration of the quinoidal unit facilitates compact π–π stacking and efficient intermolecular charge transport and (ii) quinoidal units typically have excellent π-electron delocalization and a strong intramolecular charge-transfer effect, resulting in reduced optical bandgaps and elevated absorption coefficients.

Thiophene and its derivatives play a crucial role in the semiconductor electronic revolution, namely organic electronics, and thiophene-containing polymers and oligomers are prominent in this field in applications that include thin-film transistors, OLEDs and organic photovoltaics.[32] 4,4-Dihexyl-4*H*-cyclopenta[2,1-*b*:3,4-*b*′]dithiophene (CPDT) is a versatile

[a] Department of Physics and Electronic Communication, The LNM Institute of Information Technology, Jamdoli, Jaipur (Rajasthan) 302031, India. E-mail: gdsharma@lnmiit.ac.in, gdsharma273@gmail.com
[b] Instituto de Nanociencia, Nanotecnología y Materiales Moleculares (INAMOL), Universidad de Castilla-La Mancha, Campus de la Fábrica de Armas, 45071 Toledo, Spain. E-mail: Fernando.Langa@uclm.es, Pilar.Cruz@uclm

† Electronic supplementary information (ESI) available. See DOI: https://doi.org/10.1039/d5tc00724k

component of opto-electronic materials due to the completely planar nature of the fused-dithiophene, the excellent π-electron donor ability and the possibility of incorporating alkyl chains to afford solubility.[33,34]

Tetracyanoquinodimethane oligothiophenes have been widely used in the field of organic conjugated molecules[35,36] and some of us prepared a quinoidal derivative of bis-CPDT-vinylene that had novel electronic properties and potential applications in organic electronics.[37] We recently reported a series of bis(semiquinone) compounds with CPDT bridges of different lengths (***n*-QDT**) that were encapsulated with benzoquinone to give systems that evolve from closed-shell (n = 1) to full diradical (n = 3).[38]

The majority of efficient OSC active layers still have the BHJ structure proposed by Heeger and co-workers.[18] The absorption spectra of most polymer donors are in the short wavelength region while the absorption spectra of most NFAs are in the long wavelength and near-infrared regions and, as a consequence, the absorption spectrum of the binary BHJ active layer makes it difficult to cover the entire solar spectrum. This limitation hinders the effective absorption of solar light, which in turn limits any improvement in photocurrent. In an effort to overcome this challenge, a ternary approach has been developed that involves BHJ active layers with either two donors and one acceptor or one donor and two acceptors. This approach has led to significant enhancements in the PCE of OSCs.[39,40] The third component (donor or acceptor) of effective ternary OSCs must have a complementary absorption profile, cascade energy level alignment, and strong compatibility with the existing binary host blend.

We report here the use in OSCs of the shortest member of the aforementioned series, namely **QDT1**,[38] which has a stable quinoidal closed-shell form. **QDT1** was employed as a medium-bandgap non-fused small molecule acceptor (NFSMA) for ternary organic solar cells along with PBDB-T as a donor and Y6 as an acceptor. **QDT1** showed excellent performance as the third component. The OSC based on PBDB-T:**QDT1**:Y6 gave a PCE value of 13.31%, which exceeds that of binary counterparts (11.17 and 7.52% for PBDB-T:Y6 and PBDB-T:**QDT1**, respectively). PL and TRPL spectroscopy revealed that a highly efficient FRET occurred between **QDT1** and Y6, which led to more efficient exciton diffusion and subsequent exciton dissociation. TPV and TPC measurements revealed that the introduction of **QDT1** into the host PBDB-T:Y6 material led to faster charge extraction and longer charge carrier lifetime, which in turn led to the suppression of both bimolecular and trap-assisted recombination. This resulted in improvements in the J_{SC}, FF and overall PCE. Moreover, the OSC based on PBDB-T:**QDT1** gave a PCE greater than 23% under white light LED illumination.

Results and discussion

Electronic and theoretical studies

The skeletal structures of polymer PBDB-T, **QDT1**, and Y6 are illustrated in Fig. 1a. **QDT1** was prepared as reported previously.[38] The spectrum of a dilute solution of **QDT1** in CH_2Cl_2

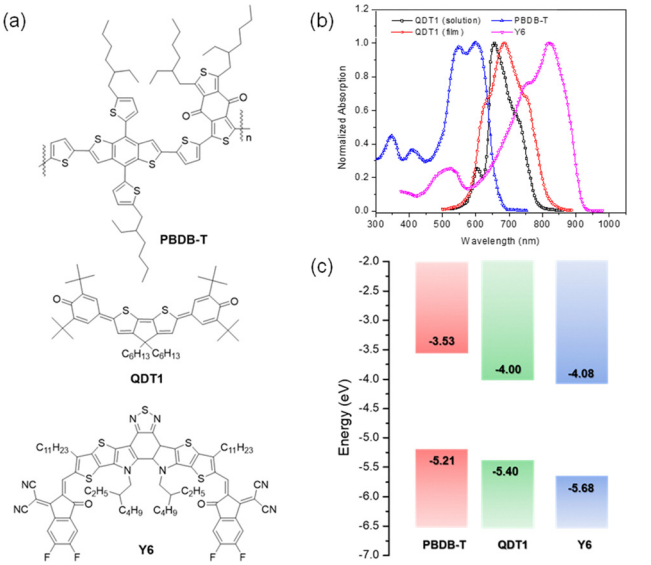

Fig. 1 (a) Chemical structures of PBDB-T, **QDT1**, and Y6. (b) UV-Vis-NIR spectra of **QDT1** in solution, **QDT1** in thin film, PBDB-T in thin film, and Y6 in thin film. (c) Schematic energy level diagrams of materials used in photovoltaic devices.

shows an absorption maximum at 656 nm and an absorption edge at around 780 nm (Fig. 1b). In thin film, a broader absorption band with a maximum of 676 nm and a shoulder at 780 nm is observed. This bathochromic shift indicates a highly ordered and compact J-aggregate arrangement of molecules in the solid state, which enhances the excitonic interactions. The absorption edge in the thin film is observed at 850 nm, and this corresponds to an optical bandgap of 1.45 eV. The thin film UV-Vis absorption spectra of PBDB-T, **QDT1**, and Y6 cast from chloroform solution are shown in Fig. 1b. Both PBDB-T and Y6 show strong absorption in the regions of 350–700 nm and 600–900 nm. **QDT1** displays maximum absorption at 676 nm, whilst its predominant absorption ranges from 500–850 nm. Both spectra combine to give a complementary absorption spectrum that should enable substantial photon harvesting with the host PBDB-T and Y6. This system is expected to have a strong capability for photon harvesting and potentially lead to a higher J_{SC} value in the ternary OSCs.

The energy levels of PBDB-T, Y6, and **QDT1**, as estimated by electrochemistry, are depicted in Fig. 1c. The results infer that the LUMO (−4.00 eV) and HOMO (−5.40 eV) energy levels of **QDT1** are located between those of PBDB-T (−3.53/−5.21 eV) and Y6 (−4.08/−5.68 eV), thus establishing a cascading energy arrangement. This arrangement could help to facilitate efficient charge transfer at the D/A interfaces, modulate the energy losses and promote charge separation.[41,42] Furthermore, the relatively upshifted LUMO energy level of **QDT1** (−4.00 eV), when compared to that of Y6 (−4.08 eV), indicates possible advantages in achieving greater V_{OC} values for ternary OSCs.

The most stable geometry of **QDT1** (Fig. S1a, ESI†) was calculated using a DFT (B3LYP) method with a 6-31G* basis set. These calculations indicate the high planarity of the quinoidal system (**QDT1**). The molecular dipole moments of Y6 and **QDT1**

were also calculated (Fig. S1b, ESI†) and it was found that **QDT1** has a significantly higher dipole moment (4.859 D) than Y6 (0.523 D). The main difference in these dipole moments lies along the *y*-axis. In the case of Y6, there are polar groups on both sides (up and down) of the *x*-axis and this arrangement results in compensation of the dipole moments on both sides. In **QDT1**, however, all the polar groups are aligned along the 'north' axis. The intermolecular packing interactions[43,44] are affected by large differences in the dipole moments between **QDT1** and Y6. The electrostatic potential (ESP) distributions of Y6 and **QDT1** were computed (Fig. S2, ESI†) and the results show that the highest energy value is in the CPDT moiety and the lowest in the quinone terminal units.

Photovoltaic performance

As depicted in Fig. 1c, the LUMO offset between PBDB-T and either **QDT1** or Y6 is sufficiently above the threshold force required for the dissociated excitons from the PBDB-T to break it into free charge carriers. This situation facilitates the subsequent transfer of electrons from the donor to the acceptor in both PBDB-T:Y6 and PBDB-T:**QDT1** BHJ active layers. There is adequate HOMO offset between PBDB-T and Y6 to ensure that there is effective hole transfer from Y6 to PBDB-T which is followed after the dissociation of excitons generated in Y6. PBDB-T and **QDT1** assure a HOMO offset of about 0.19 eV between them. To gain information about exciton dissociation after their generation, and transfer of holes from HOMO of **QDT1** to HOMO of PBDB-T, the photoluminescence (PL) spectra of pristine **QDT1** film and its blend with PBDB-T were compared and shown in Fig. S3 (ESI†). We can see PL quenching of **QDT1** when blended with PBDB-T. This only suggests effective exciton dissociation and subsequent transfer of holes from **QDT1** to PBDB-T. The processes occur though the HOMO offset is less. Such exciton dissociation and charge transfer are often reported for OSCs in which NFSMA, and polymer or small molecule donors are employed.[45–47]

The OSCs were fabricated with the conventional architecture of binary and ternary OSCs comprising ITO-coated glass as TCO, PEDOT:PSS as HTL, PFN-Br as ETL and Ag (100 nm) as anode (which was deposited by thermal evaporation technique). All the processes were done in ambient conditions. PBDB-T and Y6 or **QDT1** were used as the polymer donor and acceptor, respectively. All devices were prepared by spin-coating solutions of the components with a PBDB-T : Y6 weight ratio of 1 : 1.2. A concentration of 14 mg mL^{-1} was maintained. The detailed procedure for device fabrication is provided in the ESI.† The ternary OSCs were prepared by adding different amounts of **QDT1**. 1-Chloronaphthalene (CN) at 0.25 vol% was included as a solvent additive. The resulting thin films were allowed for thermal annealing at 110 °C for about 5 minutes. The obtained devices were characterized under 1 sun conditions (AM 1.5G spectra).

The current–voltage (*J*–*V*) characteristics of the optimized binary (PBDB-T:**QDT1** or PBDB-T:Y6) and ternary (PBDB-T:**QDT1**:Y6) devices are depicted in Fig. 2a and their photovoltaic parameters are tabulated in Table 1. The binary OSCs comprising PBDB-T:Y6 and PBDB-T:**QDT1** yield efficiencies of 11.17% and 7.52%, respectively. The dipole moment of QDT1 is higher than that of Y6, and, as a consequence, the exciton binding energy of the **QDT1** system is lower. In this case, a lower driving force is required for the dissociation of excitons, and hence the higher value of V_{OC} for the OSCs based on **QDT1**. Moreover, the inclusion of 20% wt of **QDT1** in PBDB-T:Y6 blends gave PBDB-T : **QDT1** : Y6 (1 : 0.2 : 1.0) ternary OSCs with a remarkable PCE value of 13.31%. This high value is due to the simultaneous increase in V_{OC} (0.836 V), J_{SC} (22.84 mA cm^{-2}) and fill factor (0.697) when compared to PBDB-T:Y6 OSCs. The **QDT1** film exhibited a complementary absorption with both PBDB-T and Y6, thus enhancing the light-harvesting capability and increasing the J_{SC} in the ternary OSC. The V_{OC} value for the ternary device is higher than the binary Y6 counterpart but still less than PBDB-T:**QDT1**. The open voltage of the BHJ-based OSC is correlated to the difference in energy levels between the LUMO of the acceptor and the HOMO of the donor. It can, therefore,

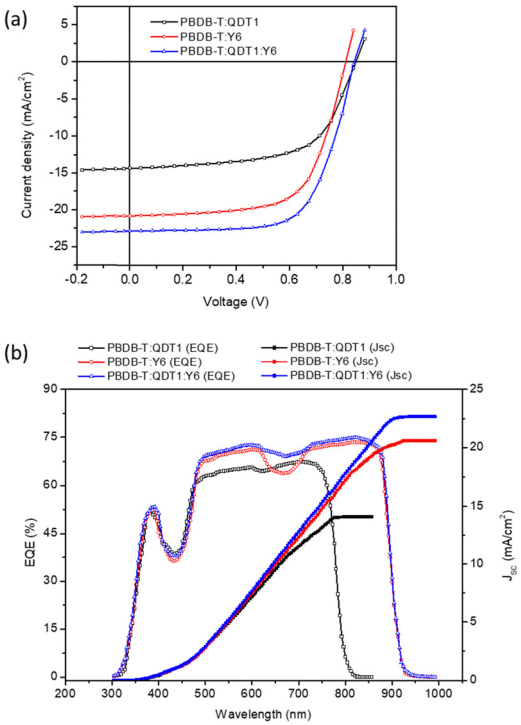

Fig. 2 (a) *J*–*V* characteristics under 1 sun condition (AM1.5G, 100 mW cm^{-2}), (b) EQE spectra of the optimized binary (PBDB-T:**QDT1** and PBDB-T:Y6) and ternary PBDB-T:**QDT1**:Y6 OSCs.

Table 1 Photovoltaic parameters of the binary and ternary OSCs based on PBDB-T as donor and **QDT1** and Y6 as acceptors

Active layer	J_{SC} (mA cm^{-2})	V_{OC} (V)	FF	PCE
PBDB-T:**QDT1**	14.36 (14.09)[a]	0.854	0.613	7.52 (7.34)[b]
PBDBT-T:Y6	20.78 (20.57)[a]	0.812	0.662	11.17 (10.97)[b]
PBDB-T:**QDT1**:Y6	22.84 (22.65)[a]	0.836	0.697	13.31 (13.06)[b]

[a] J_{SC} value obtained from the integration of EQE spectra. [b] Average value of 8 identical devices.

be envisaged that the higher V_{OC} for the ternary system, when compared to the Y6 binary counterpart, may be due to the fact that the LUMO of **QDT1** is upshifted in relation to that of Y6.

The external quantum efficiency spectra (EQE) of all the devices are displayed in Fig. 2b. The spectra of PBDB-T:**QDT1** and PBDB-T:Y6 are very similar to the UV-Vis-NIR spectra of their corresponding blends in the thin film. The EQE values of the ternary OSCs are higher than those of the PBDB-T:Y6 counterpart – particularly in the wavelength region 600–740 nm, where the absorption coefficient of **QDT1** is high. This indicates that the incorporation of **QDT1** into PBDB-T:Y6 mixtures increases the light-harvesting ability and thus leads to a higher J_{SC} value for the ternary OSC. The J_{SC} values of the OSCs are given further validation by the EQE spectra. The J_{SC} values attained by the area of the EQE spectra closely match the J_{SC} measured from the J–V curves (Table 1).

The energy level difference of LUMO of the acceptor material and HOMO of the donor material gives out the V_{OC} of the bulk-hetero junction devices. Due to the same, the V_{OC} of the ternary active layer (0.836 V) lies between the two binary counterparts. Cyclic voltammetry measurements on optimized Y6:**QDT1** blend film were done to calculate HOMO–LUMO levels and further their V_{OC} dependence. The HOMO and LUMO energy levels of the optimized acceptor blend are −5.48 and −4.04 eV, respectively. These values lie between those of Y6 and **QDT1**, which results in an increase in the charge transfer (CT) state (ECT) with dark current density being in a suppressed state for ternary blends.[48,49] Moreover, the V_{OC} values of the ternary OSCs increase as the concentration of **QDT1** increases (Table S1, ESI†), a trend that is consistent with the formation of an alloy between the two acceptors.[50] Thus, the incorporation of **QDT1** as a third component can increase the open circuit voltage (V_{OC}).[51,52]

Exciton generation and charge recombination dynamics

The exciton dissociation (P_{diss}) probability was investigated by examining plots of the photocurrent density (J_{ph}) variation with effective voltage (V_{eff}) (Fig. 3). The estimation of both the J_{ph} and V_{eff} values is described in the ESI.†

The J_{ph} value increases as V_{eff} increases and the photocurrent then becomes almost saturated when $V_{eff} > 1.8$ V. The saturation current density (J_{sat}) in the ternary OSC was found to be higher than those in the binary counterparts and this finding indicates enhanced light-harvesting ability and a more efficient exciton generation rate. The value of P_{diss} under short circuit condition was estimated using the expression $P_{diss} = J_{ph}/J_{sat}$. The P_{diss} value for the ternary OSC (0.982) is higher than that for binary counterparts (0.946 and 0.963 for PBDB-T:**QDT1** and PBDB-T:Y6, respectively) and this suggests that the ternary OSC exhibited faster dissociation of excitons into free charges and subsequent collection of them by the electrodes, which in turn contributes to the enhancement of J_{SC} and FF.[53]

The carrier dynamics of devices, including their transport, and recombination processes were evaluated by examining the J_{SC} and V_{OC} correlation with varying illumination power (P_{in}) in both binary and ternary OSCs. The slopes of V_{OC} *versus* P_{in} plots (Fig. 4a) were fitted using the expression $V_{OC} = (nkT/q)\ln P_{in}$ and

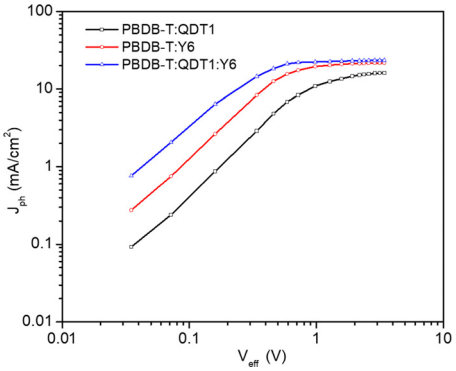

Fig. 3 Plot of photocurrent density (J_{ph}) with effective voltage (V_{eff}) for binary (PBDB-T:**QDT1** and PBDB-T:Y6) and ternary (PBDB-T:**QDT1**:Y6) OSCs.

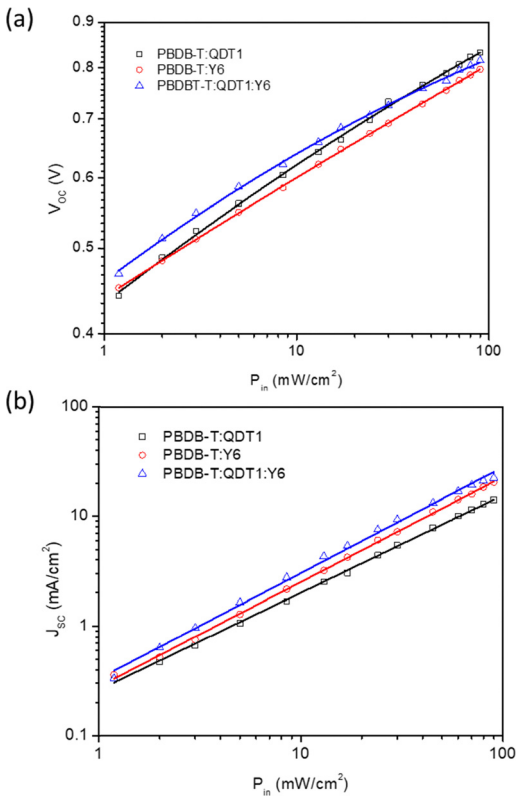

Fig. 4 Dependence of (a) V_{OC} and (b) J_{SC} with P_{in} for optimized binary (PBDB-T:**QDT1** and PBDB-T:Y6) and ternary (PBDB-T:**QDT1**:Y6) OSCs.

the values were 1.45, 1.32 and 1.23kT/q for PBDB-T:**QDT1**, PBDB-T:Y6 and PBDB-T:**QDT1**:Y6 OSCs, respectively. Compared to binary OSCs, the lower slope obtained for the ternary counterpart suggests that trap-assisted recombination was lower in the ternary OSC, which leads to improved charge transport and enhanced J_{SC} and FF.[54] The J_{SC}–P_{in} curves (Fig. 4b) were fitted using the relationship $J_{SC} \propto (P_{in})^{\alpha}$, where α is used to determine the degree of bimolecular recombination. The α values calculated for ternary structure is 0.974, while binary counterparts PBDB-T:**QDT1** (0.912), PBDB-T:Y6 (0.959),

has a slightly lower values. The higher α value obtained for the ternary device, when compared to the binary counterparts, indicates relatively weak bimolecular recombination in the ternary OSC.[55,56]

The transient photovoltage (TPV) was employed for assessing the carrier recombination kinetics in these devices and the results are depicted in Fig. 5a. The PBDB-T:**QDT1**:Y6 ternary device exhibited a longer carrier lifetime (7.75 μs) than the binary counterparts (5.38 μs and 3.76 μs for PBDB-T:Y6 and PBDB-T:**QDT1**, respectively). The longer carrier lifetime attributes to a longer transport distance for photogenerated charge carriers, and this is only possible due to less recombination, which in turn enhances both J_{SC} and FF.[57] Moreover, transient photocurrent (TPC) measurements (Fig. 5b) demonstrate that the PBDB-T:**QDT1**:Y6 device yielded the shortest photocurrent decay time of 0.784 μs when compared to PBDB-T:**QDT1** (1.26 μs) and PBDB-T:Y6 (0.965 μs). This difference signifies that the ternary devices have enhanced charge extraction efficiency. The high carrier extraction eased to reduce carrier recombination inside the active layer and this ensures timely extraction and transport of a greater number of photogenerated carriers to the electrodes, thereby improving both J_{SC} and FF.[58]

The charge transport kinetics in the active layers were further examined by carrying out space charge limited current (SCLC) measurements using hole and electron-only devices (Fig. S4a and b, ESI†). The addition of **QDT1** led to an increase in both hole mobility (μ_h) and electron mobility (μ_e) for the PBDB-T:**QDT1**:Y6 device when compared with the PBDB-T:Y6 devices. The μ_h and μ_e values increased from 4.56×10^{-4} to 5.67×10^{-4} cm^2 V^{-1} s^{-1} and from 3.42×10^{-4} to 4.78×10^{-4} cm^2 V^{-1} s^{-1}, respectively. The enhanced charge carrier mobilities and more balanced $\mu_h/\mu_e = 1.19$ in the PBDB-T:**QDT1**:Y6 ternary film, which suppresses the charge recombination, is consistent with the enhanced FF for the ternary OSC. These findings clearly show that **QDT1**, as a guest acceptor, can simultaneously aid in exciton dissociation and carrier generation, thus significantly enhancing the J_{SC} and FF of the OSC.

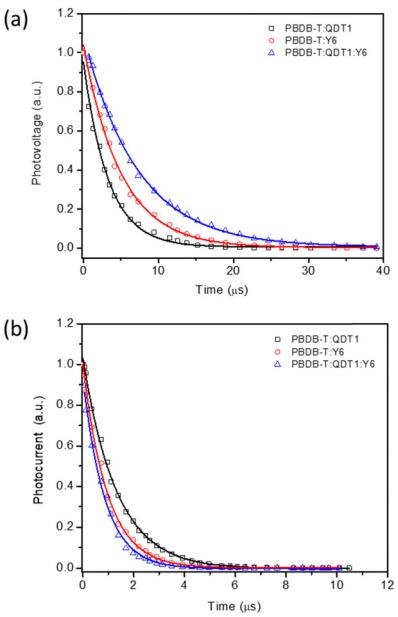

Fig. 5 (a) TPV and (b) TPC curves for the binary (PBDB-T:**QDT1** and PBDB-T:Y6) and ternary (PBDB-T:**QDT1**:Y6) OSCs.

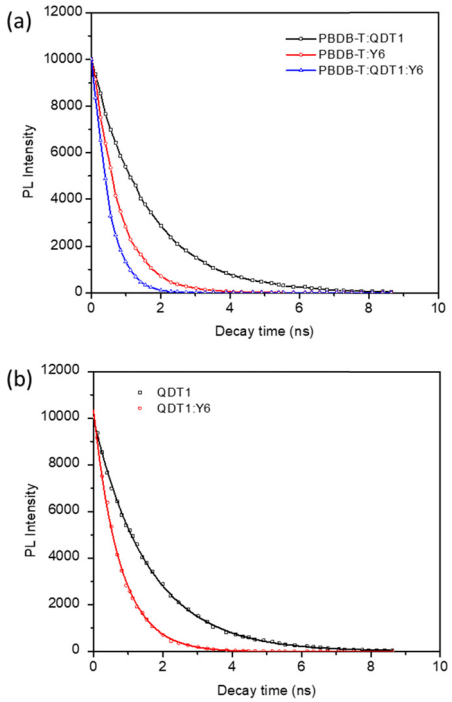

Fig. 6 (a) TRPL plots for PBDB-T:**QDT1**, PBDB-T:Y6 and PBDB-T:**QDT1**:Y6 and (b) **QDT1** and **QDT1**:Y6.

TRPL spectroscopy is a technique that is used to obtain information about the exciton diffusion and exciton dissociation in the devices and selected spectra are shown in Fig. 6. The decay time represents the exciton dissociation at the D/A interface and exciton diffusion towards the interfaces.[59] Compared with binary blends (0.886 ns and 0.781 ns for **QDT1** and Y6-based blends, respectively), the shorter decay time (0.506 ns) measured for the ternary blend indicates faster exciton diffusion and transfer behaviour in ternary OSCs. These properties result in increased J_{SC} and PCE values.

Energy loss analysis

Energy loss (E_{loss}) analysis of binary and ternary devices was performed in an effort to understand the V_{OC} enhancement in the ternary OSCs. E_{loss} is expressed as $E_{loss} = E_g - V_{OC}$, where E_g is the optical energy bandgap of the blend film, which can be estimated from the peak observed 1st derivative of EQE of the OSC (Fig. S5, ESI†). The E_g values for the blends were estimated to be 1.58, 1.38 and 1.38 eV for PBDB-T:**QDT1**, PBDB-T:Y6 and PBDB-T:**QDT1**:Y6, respectively. The detailed E_{loss} values are shown in Table 2. In general, the E_{loss} of a solar cell can be divided into three parts: ΔE_1, ΔE_2 and ΔE_3. ΔE_1 is denoted as $E_g - qV_{OC}^{SQ}$, where V_{OC}^{SQ} represents the theoretical upper limit for the V_{OC}, as derived from Shockley–Queisser theory. This limit originates from the absorption above the bandgap[60] and its value is almost the same for all of the devices. ΔE_2 can be

Table 2 Energy loss data for the binary and ternary OSCs based on PBDB-T as donor and Y6 and **QDT1** as acceptors

Device	E_g (eV)	ΔE_1 (eV)	ΔE_2 (eV)	ΔE_3 (eV)	Total E_{loss} (eV)
PBDB-T:**QDT1**	1.58	0.255	0.0945	0.377	0.726
PBDB-T:Y6	1.38	0.249	0.0876	0.231	0.568
PBDB-T:**QDT1**:Y6	1.38	0.249	0.076	0.219	0.544

determined by the expression $\Delta E_2 = q(V_{OC}^{SQ} - V_{OC}^{rad})$ and it represents the loss of radiation recombination below the bandgap, which is determined by the degree of energy disorder and recombination.[61] The ΔE_2 value obtained for the ternary device is significantly lower than that for the binary device – a finding that suggests minimal energy disorder in the ternary device. ΔE_2 can also be quantified by a parameter called the Urbach energy (E_U), where a low E_U value signifies low energy disorder. The FTPS-normalized EQE (Fig. S5, ESI†) with Urbach's rule[62,63] indicates that the E_U of the ternary device is lower (26.65 meV) than that of the binary devices (31.43 meV and 28.25 meV for **QDT1** and Y6, respectively). The lower E_U value is mainly attributed to the enhanced molecular aggregation, reduced reorganization energy and energy disorder in the ternary blend film.[64] ΔE_3 represents the non-radiative loss term, which originates from the recombination of charge carriers in the device. The ΔE_3 value for the ternary system is 0.219 eV, which is lower than the values for the binary counterparts. The lower ΔE_3 value for ternary OSC is related to suppression of the charge carrier recombination.

Energy and charge transfer mechanisms in the ternary device

It can be seen from Fig. 7a that the steady state PL of **QDT1** has significant overlap with the absorption spectrum of Y6. This observation indicates that Förster resonance energy transfer (FRET) occurs from the medium-bandgap acceptor **QDT1** to the low-bandgap acceptor Y6 – a phenomenon that is observed in many ternary OSCs. In an effort to obtain more information about the energy transfer, the steady state PL spectra of **QDT1**, Y6 and a **QDT1**:Y6 blend were investigated. It can be seen from Fig. 7b that the emission peaks of **QDT1** and Y6 are located at 816 nm and 920 nm, respectively. The incorporation of **QDT1** with Y6 led to almost complete quenching of the PL emission intensity of **QDT1** along with a simultaneous increase in the PL intensity of Y6. This behavior indicates an efficient energy transfer from **QDT1** to Y6. An alternative approach to confirm the energy transfer between **QDT1** and Y6 involves creating solar cells with **QDT1**:Y6 (0.2 : 1.0) and pristine **QDT1** or Y6 as the active layers without a donor, respectively. The J_{SC} value of the **QDT1**:Y6-based OSC is 0.68 mA cm^{-2}, which is lower than the values for both pristine **QDT1** (0.89 mA cm^{-2}) and Y6 (1.05 mA cm^{-2}). These values imply that charge transfer between **QDT1** and Y6 is negligible.

In accordance with FRET theory, the lifetimes of energy donors in an excited state decrease with increasing acceptor concentration since FRET is an additional non-radiative decay channel for a donor in the system.[65] TRPL spectroscopy was used to investigate the energy transfer from **QDT1** to Y6

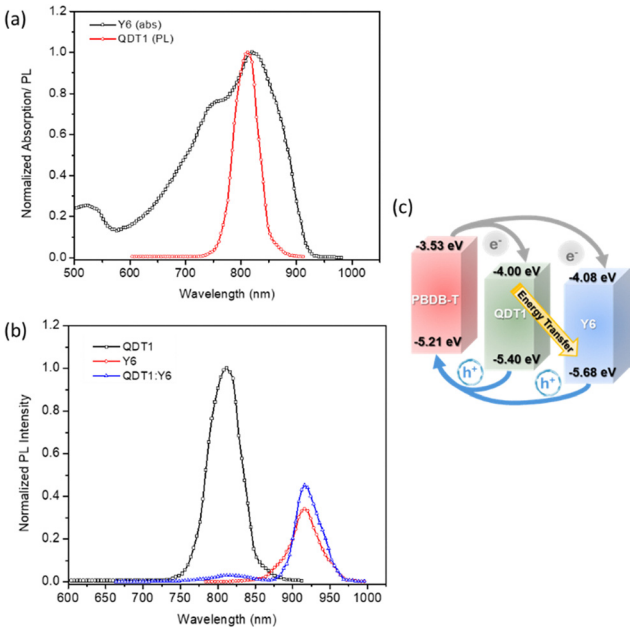

Fig. 7 (a) Absorption spectra and PL spectra of Y6 and **QDT1**, respectively, (b) PL spectra of pristine **QDT1**, Y6 and **QDT1**:Y6, and (c) energy and charge transfer in the ternary device.

(excitation wavelength of 690 nm and probing 830 nm emission). The average lifetime of pristine **QDT1** was 1.55 ns, which is markedly decreased to 0.66 ns for the **QDT1**:Y6 (0.2 : 1.0) film. The energy transfer efficiency (η) from the energy donor (**QDT1**) to the energy acceptor (Y6) can be estimated using the following expression: $\eta = 1 - (\tau_{DA}/\tau_D)$, where τ_D and τ_{DA} denote the fluorescence lifetime of the donor with and without the acceptor, respectively. **QDT1** and Y6 act as energy donor and energy acceptor, respectively. On using the above expression, the energy transfer efficiency was calculated to be 57.3% and this is consistent with the overlap of the absorption spectrum of Y6 and PL spectrum of the **QDT1**. The energy transfer and charge transfer mechanisms are illustrated in Fig. 7c. It can be concluded that there is a balance between the exciton dissociation process and the energy transfer process in the optimized ternary OSC.[66]

The surface morphologies of PBDB-T:Y6 and PBDB-T:**QDT1**:Y6 blends were investigated by atomic force microscopy (AFM) (Fig. S6, ESI†) in an attempt to elucidate why the ternary OSC gave a high PCE value. Both blends gave smooth films that had low surface roughness. The ternary PBDB-T:**QDT1**:Y6 film showed slightly higher roughness (2.34 nm) compared to the binary PBDB-T:Y6 counterpart (2.09 nm) and this is mainly due to the improved molecular aggregation. Higher surface roughness is beneficial for both high J_{SC} and FF values in OSCs.[67]

The surface morphologies of PBDB-T:Y6 and PBDB-T:**QDT1**:Y6 blends were investigated by atomic force microscopy (AFM) (Fig. S6, ESI†) in an attempt to elucidate why the ternary OSC gave a high PCE value. Both blends gave smooth films that had low surface roughness. The ternary PBDB-T:**QDT1**:Y6 film showed slightly higher roughness (2.34 nm) compared to the

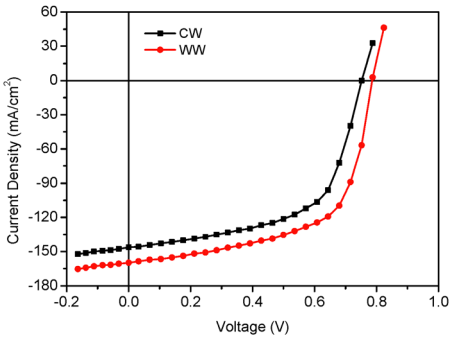

Fig. 8 *J–V* characteristics of the OSC based on PBDB-T:**QDT1** under illumination with stanard white (SW) LED (1000 lux).

Table 3 Photovoltaic parameters of OSCs based on PBDB-T:**QDT1** under 1000 lux LED illumination

LED	J_{SC} (μA cm^{-2})	V_{OC} (V)	FF	PCE (%)
CW	146.34	0.752	0.587	21.51
SW	159.45	0.786	0.602	23.76

binary PBDB-T:Y6 counterpart (2.09 nm) and this is mainly due to the improved molecular aggregation. Higher surface roughness is beneficial for both high J_{SC} and FF values in OSCs.[67]

A great deal of research has been carried out in recent years on OSCs for indoor applications[68–70] and the PCE has been boosted up to 30%.[71,72] Both PBDB-T and **QDT1** showed strong absorptions up to 800 nm and this is very similar to the emission spectrum of white LEDs. As a consequence, the *J–V* characteristics were measured under different absorption spectra. The binary and ternary OSCs were also tested under indoor light illumination (white LED, 1000 lux) using standard white (SW) and cool white (CW). The detail of the *J–V* measurements is summarized in ESI.† We have measured the intensity of indoor light by luxmeter and it is 300.3 and 317.5 μW cm^{-2} for SW and CW LEDs, respectively.[73] The *J–V* characteristics are shown in Fig. 8 and the corresponding photovoltaic parameters are compiled in Table 3. The PCE values of OSCs based on indoor light illumination exceeded 23% under SW LED, thus demonstrating the potential applications of medium-bandgap NFAs along with wide-bandgap polymer donors for indoor OSCs.

Conclusions

A quinoidal A–D–A non-fullerene small-molecule acceptor **QDT1** was utilized as a guest acceptor in the host binary blend PBDB-T:Y6 to fabricate ternary OSCs. It is worth highlighting that addition of only a small amount of **QDT1** can significantly improve the PCE of the ternary OSC from 11.17% to 13.31%. This improvement mainly results from the enhanced J_{SC} and FF. The mechanism was investigated by PL and TRPL studies, which showed that **QDT1** acts as an additional light absorber to harvest more photons and deliver photon energy to Y6 through FRET. In this process extra excitons were generated and then dissociated into free charge carriers, which resulted in an improvement in the J_{SC} in the ternary OSCs. Moreover, the OSCs based on PBDB-T:**QDT1** gave PCE values above 24% under indoor light illumination, thus highlighting the potential of the BHJ active layer consisting of PBDB-T and **QDT1** for applications in indoor OSCs.

Author contributions

M. P. has synthesized simple medium-bandgap quinoidal A–D–A non-fullerene acceptor **QDT1**. S. S. S. has been involved in the photovoltaic studies. P. C., F. L. and G. D. S. have directed the experiments and the interpretation of the data.

Data availability

The data supporting the findings of this study are available in the ESI† of this article.

Conflicts of interest

There are no conflicts to declare.

Acknowledgements

Financial support from the MCIN/AEI of Spain (PID2022-141687OB-I00, RED2022-134939-T and TED2021-131255B-C42), the Junta de Comunidades de Castilla-La Mancha, and European Social Funds (SBPLY/21/180501/000142) are acknowledged.

References

1 H. Yao and J. Hou, *Angew. Chem., Int. Ed.*, 2022, **61**, e202209021.
2 J. Yi, G. Zhang, H. Yu and H. Yan, *Nat. Rev. Mater.*, 2024, **9**, 46–62.
3 X. Liu, S. Xu, B. Tang and X. Song, *Chem. Eng. J.*, 2024, **497**, 154944.
4 Y. Li, X. Huang, H. K. M. Sheriff and S. R. Forrest, *Nat. Rev. Mater.*, 2023, **8**, 186–201.
5 B. Deng, Y. Li, Z. Lu, K. Zheng, T. Xu, S. Wang, X. Luo, B. Grandidier, J. Zhang and F. Zhu, *Nat. Commun.*, 2025, **16**, 597.
6 C. Zhu, H. Zheng, L. Zhao and X. Zhu, *Sci. China Mater.*, 2025, DOI: 10.1007/s40843-024-3210-y.
7 C. Zhang, R. Yu, Q. Lv, S. Li, H. Yuan, B. Huang and Z. Tan, *ChemSusChem*, 2025, **18**, e202401138.
8 Q. Wu, S. Ding, A. Sun and Y. Xia, *Mater. Today Chem.*, 2024, **41**, 102290.
9 T. Yu and D. Ma, *Sol. RRL*, 2024, **8**, 2300751.
10 J. Wang, Y. Xie, K. Chen, H. Wu, J. M. Hodgkiss and X. Zhan, *Nat. Rev. Phys.*, 2024, **6**, 365–381.
11 D. Luo, W. Jang, D. D. Babu, M. S. Kim, D. H. Wang and A. K. K. Kyaw, *J. Mater. Chem. A*, 2022, **10**, 3255–3295.
12 Y. Jiang, S. Sun, R. Xu, F. Liu, X. Miao, G. Ran, K. Liu, Y. Yi, W. Zhang and X. Zhu, *Nat. Energy*, 2024, **9**, 975–986.

13 C. Guo, Y. Sun, L. Wang, C. Liu, C. Chen, J. Cheng, W. Xia, Z. Gan, J. Zhou, Z. Chen, J. Zhou, D. Liu, J. Guo, W. Li and T. Wang, *Energy Environ. Sci.*, 2024, **17**, 2492–2499.
14 Y. Sun, L. Wang, C. Guo, J. Xiao, C. Liu, C. Chen, W. Xia, Z. Gan, J. Cheng, J. Zhou, Z. Chen, J. Zhou, D. Liu, T. Wang and W. Li, *J. Am. Chem. Soc.*, 2024, **146**, 12011–12019.
15 S. Wang, S. Wang, J. Wang, N. Yu, J. Qiao, X. Xie, C. Li, M. S. Abbasi, R. Ding, X. Zhang, Y. Han, G. Lu, J. Zhang, X. Hao, Z. Tang, Y. Cai and H. Huang, *Adv. Energy Mater.*, 2025, 2405205.
16 F. Furlan and N. Gasparini, *Nat. Mater.*, 2025, **24**(3), 336–337.
17 H. Chen, Y. Huang, R. Zhang, H. Mou, J. Ding, J. Zhou, Z. Wang, H. Li, W. Chen, J. Zhu, Q. Cheng, H. Gu, X. Wu, T. Zhang, Y. Wang, H. Zhu, Z. Xie, F. Gao, Y. Li and Y. Li, *Nat. Mater.*, 2025, **24**, 444–453.
18 G. Yu, J. Gao, J. C. Hummelen, F. Wudl and A. J. Heeger, *Science*, 1995, **270**, 1789–1791.
19 W. Ma, C. Yang, X. Gong, K. Lee and A. J. Heeger, *Adv. Funct. Mater.*, 2005, **15**, 1617–1622.
20 H. Huang, Q. Guo, S. Feng, C. Zhang, Z. Bi, W. Xue, J. Yang, J. Song, C. Li, X. Xu, Z. Tang, W. Ma and Z. Bo, *Nat. Commun.*, 2019, **10**, 3038.
21 P. Jiang, Y. Liu, J. Song and Z. Bo, *Acc. Chem. Res.*, 2024, **57**, 3419–3432.
22 X. Zhang, X. Gu and H. Huang, *Acc. Chem. Res.*, 2024, **57**, 981–991.
23 R. Yu, S. Li, H. Yuan, Z. Yang, S. Jin and Z. Tan, *J. Phys. Chem. Lett.*, 2024, **15**, 2781–2803.
24 D.-L. Ma, Q.-Q. Zhang and C.-Z. Li, *Angew. Chem., Int. Ed.*, 2023, **62**, e202214931.
25 D. Li, H. Zhang, X. Cui, Y.-N. Chen, N. Wei, G. Ran, H. Lu, S. Chen, W. Zhang, C. Li, Y. Liu, Y. Liu and Z. Bo, *Adv. Mater.*, 2024, **36**, 2310362.
26 Y. Shao, R. Sun, W. Wang, X. Yang, C. Sun, Y. Li and J. Min, *Sci. China: Chem.*, 2023, **66**, 1101–1110.
27 H. Tan, W. Fan, M. Zhu, J. Zhu, X. Wang, M. Xiao, R. Yang, W. Zhu and J. Yu, *Small*, 2023, **19**, 2304368.
28 S. Vegiraju, G.-Y. He, C. Kim, P. Priyanka, Y.-J. Chiu, C.-W. Liu, C.-Y. Huang, J.-S. Ni, Y.-W. Wu, Z. Chen, G.-H. Lee, S.-H. Tung, C.-L. Liu, M.-C. Chen and A. Facchetti, *Adv. Funct. Mater.*, 2017, **27**, 1606761.
29 T. Du, R. Gao, Y. Deng, C. Wang, Q. Zhou and Y. Geng, *Angew. Chem., Int. Ed.*, 2020, **59**, 221–225.
30 H. Feng, B. Yin, L. Pan, X. Liu, S. Kim, Y. Zhao, X. Huang, C. Yang and C. Duan, *Chem. Commun.*, 2023, **59**, 9529–9532.
31 Z. Zhou, S. Xu and X. Zhu, *Bull. Chem. Soc. Jpn.*, 2021, **94**, 929–936.
32 I. F. Perepichka and D. F. Perepichka, *Handbook of Thiophene-Based Materials: Applications in Organic Electronics and Photonics, 2 Volume Set*, John Wiley & Sons, 2009.
33 X. Gu, X. Zhang and H. Huang, *J. Mater. Chem. A*, 2024, **12**, 17973–17991.
34 B.-H. Jiang, Y.-S. Chen, Y.-C. You, Y.-W. Su, C.-Y. Chang, H.-S. Shih, Z.-E. Shi, C.-P. Chen and K.-T. Wong, *J. Mater. Chem. C*, 2024, **12**, 12004–12014.
35 Z. Zeng, S. Lee, J. L. Zafra, M. Ishida, X. Zhu, Z. Sun, Y. Ni, R. D. Webster, R.-W. Li, J. T. López Navarrete, C. Chi, J. Ding, J. Casado, D. Kim and J. Wu, *Angew. Chem., Int. Ed.*, 2013, **52**, 8561–8565.
36 Z. Zeng, S. Lee, J. L. Zafra, M. Ishida, N. Bao, R. D. Webster, J. T. López Navarrete, J. Ding, J. Casado, D. Kim and J. Wu, *Chem. Sci.*, 2014, **5**, 3072–3080.
37 P. Mayorga Burrezo, R. Domínguez, J. L. Zafra, T. M. Pappenfus, P. de la Cruz, L. Welte, D. E. Janzen, J. T. López Navarrete, F. Langa and J. Casado, *Chem. Sci.*, 2017, **8**, 8106–8114.
38 M. Privado, S. Moles Quintero, M. Barrejón, P. de La Cruz, J. B. PM, D. Casanova, F. Langa and J. Casado, *Angew. Chem., Int. Ed.*, 2025, **64**, e202413988.
39 N. Y. Doumon, L. Yang and F. Rosei, *Nano Energy*, 2022, **94**, 106915.
40 J. Liu, X. Liu, J. Xin, Y. Zhang, L. Wen, Q. Liang and Z. Miao, *Small*, 2024, **20**, 2308863.
41 C. Sun, J.-W. Lee, C. Lee, D. Lee, S. Cho, S.-K. Kwon, B. J. Kim and Y.-H. Kim, *Joule*, 2023, **7**, 416–430.
42 L. Xie, A. Lan, Q. Gu, S. Yang, W. Song, J. Ge, R. Zhou, Z. Chen, J. Zhang, X. Zhang, D. Yang, B. Tang, T. Wu and Z. Ge, *ACS Energy Lett.*, 2023, **8**, 361–371.
43 Z. Zhang, J. Wu, J. Lin, R. Zhang, J. Lv, L. Yu, X. Guo and M. Zhang, *J. Mater. Chem. A*, 2023, **11**, 15553–15560.
44 J. Lin, Q. Guo, Q. Liu, J. Lv, H. Liang, Y. Wang, L. Zhu, F. Liu, X. Guo and M. Zhang, *Chin. J. Chem.*, 2021, **39**, 2685–2691.
45 L. Wang, C. Zhang, Z. Su, Y. Wang, W. Su, X. Man, Z. Ma, W. Zhang, C. Li, C. Yang and Z. Bo, *J. Mater. Chem. C*, 2023, **11**, 6971–6980.
46 S. Li, L. Zhan, C. Sun, H. Zhu, G. Zhou, W. Yang, M. Shi, C.-Z. Li, J. Hou, Y. Li and H. Chen, *J. Am. Chem. Soc.*, 2019, **141**, 3073–3082.
47 S. Chen, Y. Wang, L. Zhang, J. Zhao, Y. Chen, D. Zhu, H. Yao, G. Zhang, W. Ma, R. H. Friend, P. C. Y. Chow, F. Gao and H. Yan, *Adv. Mater.*, 2018, **30**, 1804215.
48 X. Ma, H. Bin, B. T. van Gorkom, T. P. A. van der Pol, M. J. Dyson, C. H. L. Weijtens, M. Fattori, S. C. J. Meskers, A. J. J. M. van Breemen, D. Tordera, R. A. J. Janssen and G. H. Gelinck, *Adv. Mater.*, 2023, **35**, 2209598.
49 G. Simone, M. J. Dyson, S. C. J. Meskers, R. A. J. Janssen and G. H. Gelinck, *Adv. Funct. Mater.*, 2020, **30**, 1904205.
50 D. Yun, S. Xuyao, S.-Y. Lee, V. V. Sharma, H. Li, S.-J. Park, Y.-H. Kim and G.-H. Kim, *ACS Appl. Energy Mater.*, 2024, **7**, 1243–1249.
51 G. Zhang, Q. Wu, Y. Duan, W. Liu, M. Zou, H. Zhou, J. Cao, R. Li, X. Xu, L. Yu and Q. Peng, *Chem. Eng. J.*, 2023, **476**, 146538.
52 J. Wang, L. Wang, R. Sun, L. Ye, B. Zhao, J. Min and S. Tan, *Chem. Eng. J.*, 2024, **492**, 152364.
53 Z. Liu and N. Wang, *J. Mater. Chem. A*, 2020, **8**, 3211–3221.
54 J. Lv, Q. Yang, W. Deng, H. Chen, M. Kumar, F. Zhao, S. Lu, H. Hu and Z. Kan, *Chem. Eng. J.*, 2023, **465**, 142822.
55 X. Chen, D. Wang, Z. Wang, Y. Li, H. Zhu, X. Lu, W. Chen, H. Qiu and Q. Zhang, *Chem. Eng. J.*, 2021, **424**, 130397.
56 M. Zhang, B. Chang, R. Zhang, S. Li, X. Liu, L. Zeng, Q. Chen, L. Wang, L. Yang, H. Wang, J. Liu, F. Gao and Z.-G. Zhang, *Adv. Mater.*, 2024, **36**, 2308606.

57 Z. Zhao, J. Zhao, S. Chung, K. Cho, W. Xu and Z. Kan, *ACS Mater. Lett.*, 2023, **5**, 1718–1726.
58 X. Sun, J. Lv, F. Wang, C. Zhang, L. Zhu, G. Zhang, T. Xu, Z. Luo, H. Lin, X. Ouyang, C. Yang, C. Yang, G. Li and H. Hu, *Adv. Energy Mater.*, 2024, **14**, 2302731.
59 K.-N. Zhang, Z.-N. Jiang, T. Wang, J.-W. Qiao, L. Feng, C.-C. Qin, H. Yin, S.-K. So and X.-T. Hao, *Nano Energy*, 2021, **79**, 105513.
60 X.-K. Chen, D. Qian, Y. Wang, T. Kirchartz, W. Tress, H. Yao, J. Yuan, M. Hülsbeck, M. Zhang, Y. Zou, Y. Sun, Y. Li, J. Hou, O. Inganäs, V. Coropceanu, J.-L. Bredas and F. Gao, *Nat. Energy*, 2021, **6**, 799–806.
61 S. Liu, J. Yuan, W. Deng, M. Luo, Y. Xie, Q. Liang, Y. Zou, Z. He, H. Wu and Y. Cao, *Nat. Photonics*, 2020, **14**, 300–305.
62 U. Rau, B. Blank, T. C. M. Müller and T. Kirchartz, *Phys. Rev. Appl.*, 2017, **7**, 44016.
63 Z. Zhang, Y. Li, G. Cai, Y. Zhang, X. Lu and Y. Lin, *J. Am. Chem. Soc.*, 2020, **142**, 18741–18745.
64 J. Li, C. Zhang, X. Sun, H. Wang, H. Hu, K. Wang and M. Xiao, *Nano Energy*, 2024, **125**, 109542.
65 J. Lakowicz, *Principles of Fluorescence Spectroscopy*, 2006, vol. 1.
66 L. Duan, Y. Zhang, R. Deng, H. Yi and A. Uddin, *ACS Appl. Energy Mater.*, 2020, **3**, 5792–5803.
67 M. Jiang, H.-F. Zhi, B. Zhang, C. Yang, A. Mahmood, M. Zhang, H. Y. Woo, F. Zhang, J.-L. Wang and Q. An, *ACS Energy Lett.*, 2023, **8**, 1058–1067.
68 S. Biswas, Y. Lee, H. Choi, H. W. Lee and H. Kim, *RSC Adv.*, 2023, **13**, 32000–32022.
69 R. Suthar, H. Dahiya, S. Karak and G. D. Sharma, *J. Mater. Chem. C*, 2023, **11**, 12486–12510.
70 X. Liu, S. Xu, B. Tang and X. Song, *Chem. Eng. J.*, 2024, **497**, 154944.
71 W. Wang, Y. Cui, Y. Yu, J. Wang, C. Wang, H. Hou, Q. Kang, H. Wang, S. Chen, S. Zhang, H. Xia and J. Hou, *Nano Energy*, 2024, **128**, 109893.
72 C. Lee, J.-H. Lee, H. H. Lee, M. Nam and D.-H. Ko, *Adv. Energy Mater.*, 2022, **12**, 2200275.
73 A. Venkateswararao, J. K. W. Ho, S. K. So, S.-W. Liu and K.-T. Wong, *Mater. Sci. Eng., R*, 2020, **139**, 100517.